S1 Data analysis and quality control of the Aurora 4000 polar nephelometer

The particle scattering coefficients were measured at three wavelengths ($\lambda_B = 450$ nm, $\lambda_G = 525$ nm, $\lambda_B = 635$ nm) using an Aurora 4000 polar nephelometer placed in the Falcon aircraft cabin behind the aerosol inlet system (in-cabin). The Aurora 4000 polar nephelometer has the unique feature of measuring the particle scattering coefficients for various angular sectors
5 (ranging from the shutter position α to $180°$), including the total particle scattering coefficient (measured when $\alpha = 0°$).

During the A-LIFE field experiment, the Aurora 4000 polar nephelometer was mounted behind an isokinetic aerosol inlet (Schöberl et al., 2023) and measured the particle scattering coefficients for four angular sectors, with $\alpha = 0°, 20°, 50°, 90°$. This configuration enabled a temporal resolution of $6 - 15$ s. A calibration with particle-free air and CO_2 was performed at the beginning of the measurement campaign and it was checked several times during and after the field experiment. The data
10 obtained from the Aurora 4000 polar nephelometer was corrected using the average of all calibration checks, following the procedure recommended by Anderson and Ogren (1998). Additionally, multiple particle-free air measurements were conducted before and during the measurement flights to verify and correct for any potential background drift resulting from alteration in conditions during the measurements or of the carrier gas. The combined uncertainty due to instrumental noise, calibration and background drift uncertainties for 1-minute data is $\sim 3\%$. The Rayleigh scattering coefficients were subtracted to obtain the
15 Aurora 4000 particle scattering coefficients ($\sigma_{\mathrm{sp},\lambda}^{\mathrm{Aurora\,4000},\,\alpha}$). All the particle scattering coefficients were converted to standard temperature and pressure (273.15 K, 1013.25 hPa).

The total particle scattering coefficients ($\sigma_{\mathrm{sp},\lambda}$) were obtained by correcting $\sigma_{\mathrm{sp},\lambda}^{\mathrm{Aurora\,4000},\,0°}$ for angular truncation and illumination as indicated in Teri et al. (2022), i.e., using the Anderson and Ogren (1998) method deploying the Scattering Ångström exponent (C_{SAE}) for cases with SAE < 2, and the Müller et al. (2012) correction C_{polar} for cases with SAE > 2. The assumed
20 uncertainties for the angular correction are 13% and 2%, respectively. A median average was performed along selected flight sequences. For flight sequences data used in this work, the uncertainties of $\sigma_{\mathrm{sp},\lambda}$ including instrumental noise, calibration and background drift uncertainties, uncertainties of the correction to standard temperature and pressure, and the truncation error uncertainty, are within $13 - 30\%$.

S2 Data analysis and quality control of the Tri-color absorption photometer (TAP)

25 The particle absorption coefficient was measured using a a tri-color absorption photometer (TAP, Brechtel) installed in the Falcon aircraft cabin behind an isokinetic aerosol inlet (Schöberl et al., 2023) inside the aircraft cabin. Measurements were taken at three different wavelengths ($\lambda_B = 465$ nm, $\lambda_G = 520$ nm, $\lambda_R = 640$ nm). The well characterized and widely used glass fiber Pallflex E70-2075W filters with a diameter of 47 mm were used (e.g., Virkkula, 2010; Davies et al., 2019). The filter was changed before each flight and the white filter check was performed according to the manufacturer indication. The
30 light transmission through the filter decreases with the sampling time from about 1 to 0.85. Any deviation from a steady decrease in the filter transmission can be attributed to variation in inlet pressure, which modify the filter optical properties during ascent and descent of the aircraft, as noted by Petzold et al. (2011). To avoid such artifact, we analyzed the TAP data exclusively for sequences at a constant altitude.

The spot area was determined to be 43.9 ± 2.3 mm^2 by measuring the diameter of each of the 10 spots with a caliber. The TAP
35 sample flow was controlled by a mass flow meter (MFM, Alicat scientific) downstream of the measurement cell and measured by an internal flow meter. The sample flow was calibrated with a bubble flow meter (Gilibrator 2, Gilian) by varying the pressure in the range $200 - 1000$ hPa. The obtained linear least square regression parameters (Slope$= 0.92$, Offset$= -0.03$, R$^2 > 0.999$) were used to correct the measured sample flow. The calculated actual volume flow rate was 1.6 ± 0.2 L/min. Data were converted to standard temperature and pressure (273.15 K; 1013.25 hPa). Data sequences with particle absorption
40 coefficient at least at one wavelength below $0.6 Mm^{-1}$ at ambient conditions were considered below the detection limit and excluded from the analysis. This decision follows the guidelines of the TAP user manual and Ogren et al. (2017).

The particle absorption coefficient was corrected for filter loading and scattering effects with the correction scheme developed by Virkkula et al. (2005) and modified by Virkkula (2010), using the particle scattering coefficient corrected for angular truncation and illumination error. This correction scheme was developed for the Particle Soot Absorption Photometer (PSAP,
45 Radiance Reasearch) and its performance was tested for the TAP by Davies et al. (2019). Their study calculated biases in the

particle absorption coefficient measured by the TAP for urban aerosol of 38 %, 37 %, and 27 % for the blue, green, and red wavelengths, respectively. We assumed an uncertainty of 40 % for all three wavelengths, considering that the wavelength of our TAP are slightly different from the TAP used by Davies et al. (2019).

We conducted additional data quality checks by comparing the particle absorption coefficient with the mass of refractory
50 black carbon (M_{rBC}) measured by a Single Particle Soot Photometer (SP2). A correlation is expected between these two quantities since black carbon is the most important aerosol absorption component (e.g., Bond et al., 2013). We found a strong correlation with $R^2 > 0.92$ for all three wavelengths when excluding data points collected at pressure conditions lower than 400 hPa (see Figure S1). Data points collected at lower pressure appeared noisier and were excluded from our data. The high correlation between the particle absorption coefficient and the mass of refractory black carbon provided further evidence of the
55 quality of the TAP data.

Additionally, we calculated the mass absorption coefficients ($\mathrm{MAC_{corr}}$) from the correlation of the two quantities. We obtained values of $19.4\,\mathrm{m^2 g^{-1}}$, $15.9\,\mathrm{m^2 g^{-1}}$, and $10\,\mathrm{m^2 g^{-1}}$ for the wavelengths blue, green, and red respectively. These values are of the order of magnitude expected in literature for black carbon. For example, Ohata et al. (2021) reported values in the range of $10.8 - 15.1\,\mathrm{m^2 g^{-1}}$ for the $\mathrm{MAC_{corr}}$ measured in the Artic for the green wavelength of ($\lambda = 550\,\mathrm{nm}$). Our values are
60 slightly higher because the particle absorption coefficient measured by the TAP instrument includes the contribution of mineral dust, which is also expected to absorb in the blue and green wavelengths.
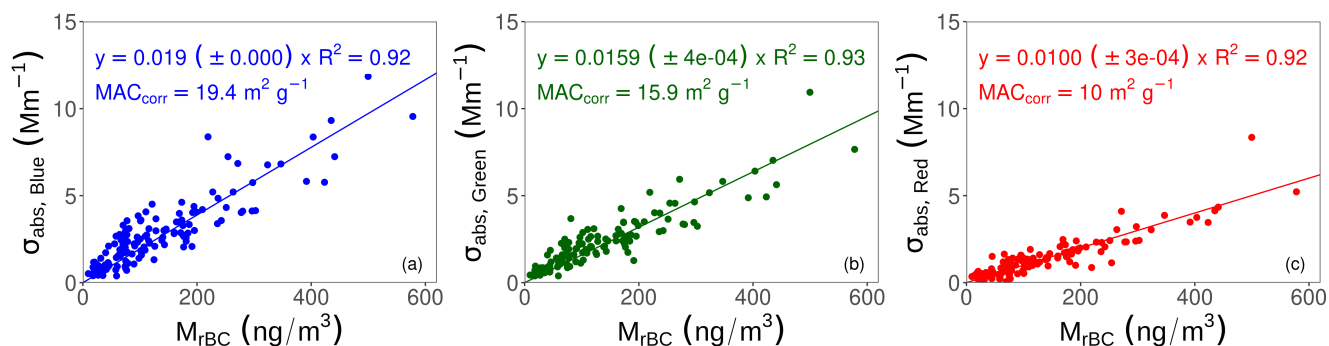
Figure S1. TAP data quality. The three panels (a,b, and c) show the comparison between the particle absorption coefficients ($\sigma_{\mathrm{sap},\lambda}$) at $\lambda = 465$, 520, and 640 nm, respectively, and the mass concentration of refractory black carbon (M_{rBC}). Results from linear regression analysis and corresponding mass absorption coefficient (MAC) values are reported on each figure.

S3 Extension of g_λ and SSA$_\lambda$ to the ambient number size distribution

The asymmetry parameter (g) and the single scattering albedo (SSA) were calculated from the particle scattering and absorption coefficients measured in the aircraft cabin behind an aerosol sampling system (see section 2.3.2 of the main text). Thus, the obtained g and SSA values are representative for the in-cabin number size distributions (NSDs). We calculated the values of g and SSA representative for the ambient NSDs ($g_{\lambda,\text{ambient}}$ and SSA$_{\lambda,\text{ambient}}$) by multiplying with a factor the measured g and SSA values ($g_{\lambda,\text{in-cabin}}$ and SSA$_{\lambda,\text{in-cabin}}$).

To calculate the correction factor to extend the measured optical properties to the ambient NSD, we performed optical simulations using the in-cabin and ambient NSDs as input of the MOPSMAP program (Gasteiger and Wiegner, 2018). The ambient NSDs were used in ambient relative humidity, while the in-cabin NDSs were used in dry conditions. The simulated optical properties were derived at three wavelengths ($\lambda_B = 450\,\text{nm}$, $\lambda_G = 525\,\text{nm}$, $\lambda_B = 635\,\text{nm}$) considering the modeled aerosol composition (see section 2.3.5 in the main text). While mineral dust particles were assumed to be spheroids with an aspect ratio distribution according to Kandler et al. (2009), the other particle types were assumed to be spherical. The dust refractive index was taken from OPAC (Hess et al., 1998) in combination with a non-absorbing fraction of 0.5 (Gasteiger and Wiegner, 2018). Refractive indices from Li (1976) for sea salt, from Moise et al. (2015) for organic matter, and from Hess et al. (1998) for soot were considered, while a value of $1.53 + 0.00i$ was assumed for sulfate. The comparison between the simulated and directly measured optical properties is out of the scope of this manuscript.

Figure S2 shows the comparisons between the simulated optical properties representative for the ambient NSDs the simulated optical properties representative for the in-cabin NSDs. For each sequence, we calculated the correction factor to extend the intensive optical properties as the ratio of the simulated property for the ambient NSD and the simulated property for the in-cabin NSD:

$$g_{\lambda,\text{ambient}} = g_{\lambda,\text{in-cabin}} \cdot \frac{\text{simulated } g_{\lambda,\text{ambient}}}{\text{simulated } g_{\lambda,\text{in-cabin}}} \tag{1}$$

$$SSA_{\lambda,\text{ambient}} = SSA_{\lambda,\text{in-cabin}} \cdot \frac{\text{simulated } SSA_{\lambda,\text{ambient}}}{\text{simulated } SSA_{\lambda,\text{in-cabin}}} \tag{2}$$
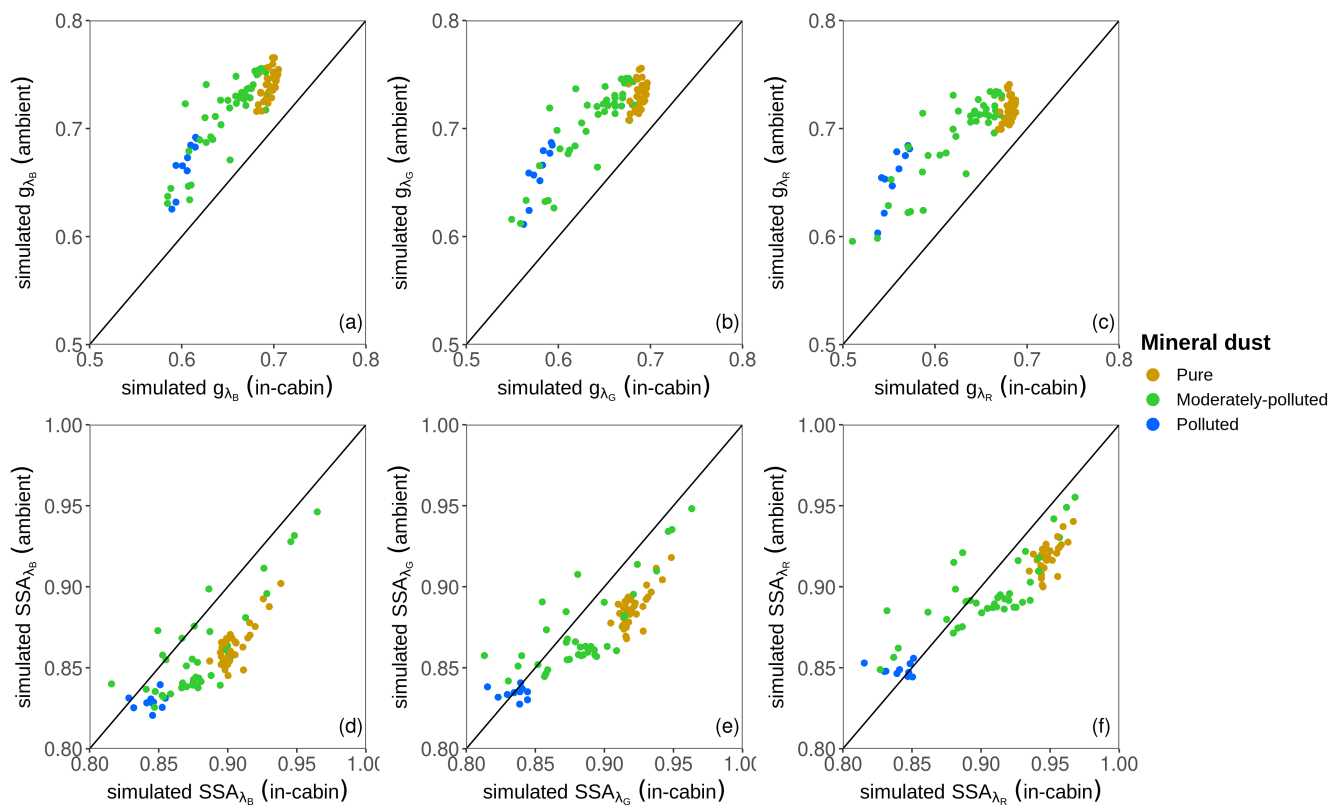
Figure S2. Simulated optical properties representative for the ambient NSD in comparison with the simulated optical properties representative for the in-cabin NSD. Panels (a,b, and c) show the comparison for the simulated $g_{\lambda,\text{ambient}}$ and the simulated $g_{\lambda,\text{in-cabin}}$ at wavelengths 450, 525, and 635 nm, respectively. Panels (d, e, and f) show the comparison for simulated $SSA_{\lambda,\text{ambient}}$ and the simulated $SSA_{\lambda,\text{in-cabin}}$ at wavelengths 450, 525, and 635 nm, respectively. The color indicates the aerosol types following the A-LIFE aerosol classification scheme. The one to one line is shown in black.

S4 Single particle chemistry analysis of samples collected during the A-LIFE field experiment

85 To support the interpretation of our results, we also used data from the single particle chemistry analysis of in-situ samples collected during the A-LIFE field experiment. An impactor sampler collecting particles with diameters < 1 μm and > 1 μm was placed in the Falcon aircraft cabin behind the aerosol inlet system (Kandler et al., 2011, 2007; Schöberl et al., 2023). Particles were collected on TEM grids and boron substrates, with sampling time varying from three to ten minutes for each sample. Subsequently, the characteristics of single particles were studied under high vacuum conditions by an automated analysis in

90 a scanning electron microscope coupled with energy-dispersive X-ray spectroscopy (SEM-EDX). Thus, the morphology and chemical composition of seven major particle-type classes were obtained (Kandler et al., 2007; Panta et al., 2023). More details on the single particle-type classification can be found in Panta et al. (2023).

The mineral dust optical properties for each sample are calculated using an empirical approach derived from Di Biagio et al. (2019) and used by Kandler et al. (2020) for particles from various mineral dust sources. The empirical relation links the total

95 iron (Fe) present in mineral dust particles as oxides with the optical properties of mineral dust particles, such as the imaginary part of the refractive index (k) and the single scattering albedo (SSA).

S4.1 Result of single particle chemistry analysis of Arabian and Saharan dust

Data from the single particle chemistry analysis of particle samples collected during sequences classified as pure and mod-

100 erately polluted Arabian and Saharan dust according to the A-LIFE aerosol classification scheme are used to support the interpretation of the result of this work.

Figure S3 shows the percentage abundances of seven particle-type classes for Arabian and Saharan dust samples. The 7 particle-type classes were obtained from 8000 particles measured under the scanning electron microscope. Figure S4 shows different element ratios for particles in Arabian and Saharan dust sequences.

105 Arabian and Saharan dust samples show a similar abundance with a higher percentage of Si-rich particles or low Al/Si ratio particles named silicate-like particles hereafter. Mineral dust particles from both source regions have $60 - 62\%$ of these silicate-like particles and the I/K ratios were similar. The most significant difference in the mineralogy composition is a higher abundance (21%) of clay-like minerals (Illite and kaolinite) from the Sahara, while the Arabian dust with a lower value of 8%. While carbonate (Calcite, Dolomite etc.) content is higher in Arabian dust (18%), a lower percentage is measured in Saharan

110 dust.

This result is in agreement with several studies conducted earlier from Saharan near-source and transported characterizing the Saharan dust particle with a higher clay mineral content (Kandler et al., 2009; Formenti et al., 2011). However, there are only limited studies in the Middle East and nearby Arabian dust sources to characterize the mineralogical characteristics of the Arabian dust (Attiya and Jones, 2020; Engelbrecht et al., 2009, 2016). All these studies show high variability in mineral dust

115 and soil mineralogy within the Arabian Peninsula, making it difficult to find an exact Arabian dust characteristic. However, compared to Saharan, a high carbonate and low clay content is common in these studies.

The percentage of iron oxides and hydroxides in Arabian dust is half that of the Saharan (3%). To obtain a more accurate iron content description, we calculated iron's total oxide weight in all mineral dust particles after Di Biagio et al. (2019). The result shows a 10% increase in the total oxide weight of iron in Saharan dust (8.7%) to Arabian dust (7.6%).

120 Since the mineral dust optical properties depend on the total iron content, this result indicates that the Saharan dust particles were more absorbing than the Arabian dust particles over the eastern Mediterranean. Indeed, the imaginary part of the refractive index (k) has a value of 0.006 for Saharan dust and 0.005 for Arabian dust. The SSA of mineral dust particles showed a 4% increase for Arabian dust compared to Saharan dust. The imaginary refractive index values of mineral dust particles are higher than the characteristics of Saharan dust as seen from other locations over Northwest Sahara or the mineral dust outflow regions

125 in the Atlantic (Kandler et al., 2011, 2007). This result might be attributed to the dust source locations depending on the season and the mixing of the sources in the eastern Mediterranean.
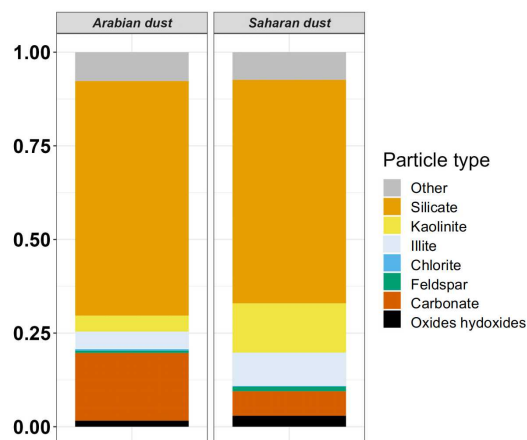
Figure S3. Results from single particle chemistry analysis. The graphs show the percentage abundances of 7 particle-type classes for Arabian and Saharan dust. The 7 particle-type classes were obtained from 8000 particles measured under the scanning electron microscope. The analyzed samples were collected during flight sequences classified as pure and moderately polluted Arabian dust and Saharan dust according to the A-LIFE aerosol classification scheme.
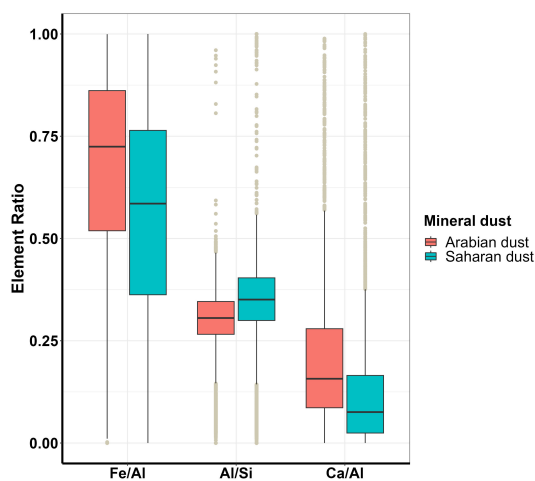
Figure S4. Element ratios (Fe/Al, Al/Si, Ca/Al) for Saharan and Arabian dust particles. The graphs show the element ratios obtained from 8000 particles measured under the scanning electron microscope. The analyzed samples were collected during flight sequences classified as pure and moderately polluted Arabian dust and Saharan dust according to the A-LIFE aerosol classification (Weinzierl et al., in prep.). The boxes represent the interquartile range (IQR $25th - 75th$), the horizontal lines the median, the whiskers the largest value that is not greater than $1.5 \cdot IQR$, and data points outside this range are shown as individual dots.
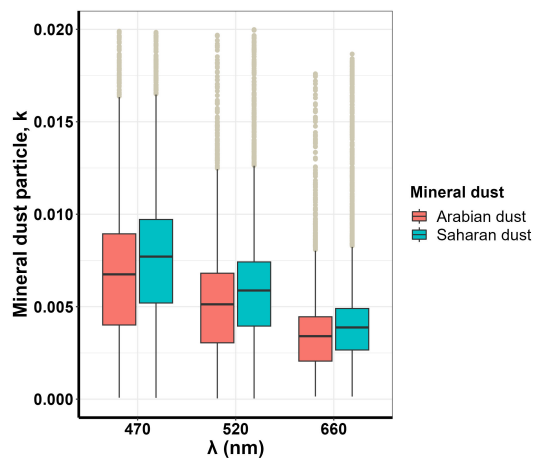
Figure S5. Spectral imaginary dust refractive index for Arabian and Saharan dust. The graph shows the median values of the imaginary part of the refractive index at three wavelengths obtained from single particle chemistry analysis. The analyzed samples were collected during flight sequences classified as pure and moderately polluted Arabian dust and Saharan dust according to the A-LIFE aerosol classification (Weinzierl et al., in prep.). The boxes represent the interquartile range (IQR $25th - 75th$), the horizontal lines the median, the whiskers the largest value that is not greater than $1.5 \cdot IQR$, and data points outside this range are shown as individual dots.

References

Anderson, T. L. and Ogren, J. A.: Determining Aerosol Radiative Properties Using the TSI 3563 Integrating Nephelometer, Aerosol Science and Technology, 29, 57–69, https://doi.org/10.1080/02786829808965551, 1998.

Attiya, Ali. A. and Jones, B. G.: Assessment of Mineralogical and Chemical Properties of Airborne Dust in Iraq, SN Applied Sciences, 2, 1614, https://doi.org/10.1007/s42452-020-03326-5, 2020.

Bond, T. C., Doherty, S. J., Fahey, D. W., Forster, P. M., Berntsen, T., DeAngelo, B. J., Flanner, M. G., Ghan, S., Kärcher, B., Koch, D., Kinne, S., Kondo, Y., Quinn, P. K., Sarofim, M. C., Schultz, M. G., Schulz, M., Venkataraman, C., Zhang, H., Zhang, S., Bellouin, N., Guttikunda, S. K., Hopke, P. K., Jacobson, M. Z., Kaiser, J. W., Klimont, Z., Lohmann, U., Schwarz, J. P., Shindell, D., Storelvmo, T., Warren, S. G., and Zender, C. S.: Bounding the Role of Black Carbon in the Climate System: A Scientific Assessment, Journal of Geophysical Research: Atmospheres, 118, 5380–5552, https://doi.org/10.1002/jgrd.50171, 2013.

Davies, N. W., Fox, C., Szpek, K., Cotterell, M. I., Taylor, J. W., Allan, J. D., Williams, P. I., Trembath, J., Haywood, J. M., and Langridge, J. M.: Evaluating Biases in Filter-Based Aerosol Absorption Measurements Using Photoacoustic Spectroscopy, Atmospheric Measurement Techniques, 12, 3417–3434, https://doi.org/10.5194/amt-12-3417-2019, 2019.

Di Biagio, C., Formenti, P., Balkanski, Y., Caponi, L., Cazaunau, M., Pangui, E., Journet, E., Nowak, S., Andreae, M. O., Kandler, K., Saeed, T., Piketh, S., Seibert, D., Williams, E., and Doussin, J.-F.: Complex Refractive Indices and Single-Scattering Albedo of Global Dust Aerosols in the Shortwave Spectrum and Relationship to Size and Iron Content, Atmospheric Chemistry and Physics, 19, 15 503–15 531, https://doi.org/10.5194/acp-19-15503-2019, 2019.

Engelbrecht, J. P., McDonald, E. V., Gillies, J. A., "Jay" Jayanty, R. K., Casuccio, G., and Gertler, A. W.: Characterizing Mineral Dusts and Other Aerosols from the Middle East—Part 2: Grab Samples and Re-Suspensions, Inhalation Toxicology, 21, 327–336, https://doi.org/10.1080/08958370802464299, 2009.

Engelbrecht, J. P., Moosmüller, H., Pincock, S., Jayanty, R. K. M., Lersch, T., and Casuccio, G.: Technical Note: Mineralogical, Chemical, Morphological, and Optical Interrelationships of Mineral Dust Re-Suspensions, Atmospheric Chemistry and Physics, 16, 10 809–10 830, https://doi.org/10.5194/acp-16-10809-2016, 2016.

Formenti, P., Schütz, L., Balkanski, Y., Desboeufs, K., Ebert, M., Kandler, K., Petzold, A., Scheuvens, D., Weinbruch, S., and Zhang, D.: Recent Progress in Understanding Physical and Chemical Properties of African and Asian Mineral Dust, Atmospheric Chemistry and Physics, 11, 8231–8256, https://doi.org/10.5194/acp-11-8231-2011, 2011.

Gasteiger, J. and Wiegner, M.: MOPSMAP v1.0: A Versatile Tool for the Modeling of Aerosol Optical Properties, Geoscientific Model Development, 11, 2739–2762, https://doi.org/10.5194/gmd-11-2739-2018, 2018.

Hess, M., Koepke, P., and Schult, I.: Optical Properties of Aerosols and Clouds: The Software Package OPAC, Bulletin of the American Meteorological Society, 79, 831–844, https://doi.org/10.1175/1520-0477(1998)079<0831:OPOAAC>2.0.CO;2, 1998.

Kandler, K., Benker, N., Bundke, U., Cuevas, E., Ebert, M., Knippertz, P., Rodríguez, S., Schütz, L., and Weinbruch, S.: Chemical Composition and Complex Refractive Index of Saharan Mineral Dust at Izaña, Tenerife (Spain) Derived by Electron Microscopy, Atmospheric Environment, 41, 8058–8074, https://doi.org/10.1016/j.atmosenv.2007.06.047, 2007.

Kandler, K., SchüTZ, L., Deutscher, C., Ebert, M., Hofmann, H., JäCKEL, S., Jaenicke, R., Knippertz, P., Lieke, K., Massling, A., Petzold, A., Schladitz, A., Weinzierl, B., Wiedensohler, A., Zorn, S., and Weinbruch1, S.: Size Distribution, Mass Concentration, Chemical and Mineralogical Composition and Derived Optical Parameters of the Boundary Layer Aerosol at Tinfou, Morocco, during SAMUM 2006, Tellus B: Chemical and Physical Meteorology, 61, 32–50, https://doi.org/10.1111/j.1600-0889.2008.00385.x, 2009.

Kandler, K., Lieke, K., Benker, N., Emmel, C., Küpper, M., Müller-Ebert, D., Ebert, M., Scheuvens, D., Schladitz, A., Schütz, L., and Weinbruch, S.: Electron Microscopy of Particles Collected at Praia, Cape Verde, during the Saharan Mineral Dust Experiment: Particle Chemistry, Shape, Mixing State and Complex Refractive Index, Tellus B: Chemical and Physical Meteorology, 63, 475–496, https://doi.org/10.1111/j.1600-0889.2011.00550.x, 2011.

Kandler, K., Schneiders, K., Heuser, J., Waza, A., Aryasree, S., Althausen, D., Hofer, J., Abdullaev, S. F., and Makhmudov, A. N.: Differences and Similarities of Central Asian, African, and Arctic Dust Composition from a Single Particle Perspective, Atmosphere, 11, 269, https://doi.org/10.3390/atmos11030269, 2020.

Li, H. H.: Refractive Index of Alkali Halides and Its Wavelength and Temperature Derivatives, Journal of Physical and Chemical Reference Data, 5, 329–528, https://doi.org/10.1063/1.555536, 1976.

Moise, T., Flores, J. M., and Rudich, Y.: Optical Properties of Secondary Organic Aerosols and Their Changes by Chemical Processes, Chemical Reviews, 115, 4400–4439, https://doi.org/10.1021/cr5005259, 2015.

Müller, T., Paixão, M., Pfeifer, S., and Wiedensohler, A.: Scattering Coefficients and Asymmetry Parameters Derived from the ! Polar Nephelometer Aurora4000!, p. 1, 2012.

Ogren, J. A., Wendell, J., Andrews, E., and Sheridan, P. J.: Continuous Light Absorption Photometer for Long-Term Studies, Atmospheric Measurement Techniques, 10, 4805–4818, https://doi.org/10.5194/amt-10-4805-2017, 2017.

Ohata, S., Mori, T., Kondo, Y., Sharma, S., Hyvärinen, A., Andrews, E., Tunved, P., Asmi, E., Backman, J., Servomaa, H., Veber, D.,
Eleftheriadis, K., Vratolis, S., Krejci, R., Zieger, P., Koike, M., Kanaya, Y., Yoshida, A., Moteki, N., Zhao, Y., Tobo, Y., Matsushita, J.,
and Oshima, N.: Estimates of Mass Absorption Cross Sections of Black Carbon for Filter-Based Absorption Photometers in the Arctic,
Atmospheric Measurement Techniques, 14, 6723–6748, https://doi.org/10.5194/amt-14-6723-2021, 2021.

Panta, A., Kandler, K., Alastuey, A., González-Flórez, C., González-Romero, A., Klose, M., Querol, X., Reche, C., Yus-Díez, J., and Pérez
García-Pando, C.: Insights into the Single-Particle Composition, Size, Mixing State, and Aspect Ratio of Freshly Emitted Mineral Dust
from Field Measurements in the Moroccan Sahara Using Electron Microscopy, Atmospheric Chemistry and Physics, 23, 3861–3885,
https://doi.org/10.5194/acp-23-3861-2023, 2023.

Petzold, A., Veira, A., Mund, S., Esselborn, M., Kiemle, C., Weinzierl, B., Hamburger, T., Ehret, G., Lieke, K., and Kandler, K.: Mixing of
Mineral Dust with Urban Pollution Aerosol over Dakar (Senegal): Impact on Dust Physico-Chemical and Radiative Properties, Tellus B:
Chemical and Physical Meteorology, 63, 619–634, https://doi.org/10.1111/j.1600-0889.2011.00547.x, 2011.

Schöberl, M., Dollner, M., Gasteiger, J., Seibert, P., Tipka, A., and Weinzierl, B.: Characterization of the Airborne Aerosol Inlet and Transport
System Used during the A-LIFE Aircraft Field Experiment, EGUsphere, pp. 1–31, https://doi.org/10.5194/egusphere-2023-439, 2023.

Teri, M., Müller, T., Gasteiger, J., Valentini, S., Horvath, H., Vecchi, R., Bauer, P., Walser, A., and Weinzierl, B.: Impact of Particle
Size, Refractive Index, and Shape on the Determination of the Particle Scattering Coefficient – an Optical Closure Study Evaluat-
ing Different Nephelometer Angular Truncation and Illumination Corrections, Atmospheric Measurement Techniques, 15, 3161–3187,
https://doi.org/10.5194/amt-15-3161-2022, 2022.

Virkkula, A.: Correction of the Calibration of the 3-Wavelength Particle Soot Absorption Photometer (3λ PSAP), Aerosol Science and
Technology, 44, 706–712, https://doi.org/10.1080/02786826.2010.482110, 2010.

Virkkula, A., Ahlquist, N. C., Covert, D. S., Arnott, W. P., Sheridan, P. J., Quinn, P. K., and Coffman, D. J.: Modification, Calibra-
tion and a Field Test of an Instrument for Measuring Light Absorption by Particles, Aerosol Science and Technology, 39, 68–83,
https://doi.org/10.1080/027868290901963, 2005.

Weinzierl, B., , , and Coauthors: The A-LIFE field experiment in the Eastern Mediterranean: highlights from the airborne observations and
insights into properties of absorbing aerosol mixtures., in prep.